Draft version March 11, 2026
Typeset using LaTeX **twocolumn** style in AASTeX7

Electron Velocity Moments in the Solar Wind. I. Calibration of the *Wind* 3DP EESA Low Detector

Lynn B. Wilson III [1], Stuart D. Bale [2,3,4], Michael L. Stevens [5], Bennett A. Maruca [6], Kristopher G. Klein [7], Mihailo M. Martinović [7], and Jason M. TenBarge [8]

[1] *NASA Goddard Space Flight Center, Heliophysics Science Division, Greenbelt, MD, USA.*
[2] *Physics Department, University of California, Berkeley, CA 94720-7300, USA.*
[3] *Space Sciences Laboratory, University of California, Berkeley, CA 94720-7450, USA.*
[4] *The Blackett Laboratory, Imperial College London, London, SW7 2AZ, UK*
[5] *Harvard-Smithsonian Center for Astrophysics, Harvard University, Cambridge, MA, USA.*
[6] *Department of Physics & Astronomy, University of Delaware, Newark, DE, USA.*
[7] *Lunar and Planetary Laboratory, University of Arizona, Tucson, AZ 85721, USA.*
[8] *Department of Astrophysical Sciences, Princeton University, Princeton, NJ 08544, USA.*

(Received March 11, 2026; Revised N/A; Accepted N/A)

Submitted to ApJS

ABSTRACT

Calibrated measurements of electron velocity distribution functions (VDFs) are necessary to characterize fluid and kinetic processes in weakly collisional and nearly collisionless plasmas such as the solar wind. Therefore, we analyzed 3,996,051 electron VDFs observed by the *Wind* 3DP thermal electron detector near 1 astronomical unit (au) between January 1, 2005 and November 25, 2017. The data were calibrated for each electron VDF to produce accurate velocity moments in the solar wind. This is the first full solar cycle coverage electron velocity moment dataset in the near-Earth solar wind. Herein (Paper I) we discuss the calibration process/algorithms and the velocity moment constraints, uncertainties, and resulting public dataset. In the second paper (Paper II), we statistically analyze the electron velocity moment dataset.

Keywords: plasmas — (Sun:) solar wind

1. BACKGROUND AND MOTIVATION

Electron velocity distribution functions (VDFs) in the solar wind are a difficult measurement to properly calibrate (e.g., J. Geach et al. 2005; V. Génot & S. Schwartz 2004; B. Lavraud & D. E. Larson 2016; M. P. Pulupa et al. 2014; C. S. Salem et al. 2001, 2003, 2023; E. E. Scime et al. 1994; P. Song et al. 1997). As a consequence, there are limited electron velocity moments in the near-Earth solar wind that have been properly calibrated. Note, however, that there are plenty of very accurate electron velocity moments in the magnetosheath (e.g., D. J. Gershman et al. 2017, 2019).

The lack of properly calibrated electron VDFs from instruments designed to measure the solar wind in the near-Earth space is a major obstacle for furthering our understanding of the solar wind's evolution. There are several primary reasons for this difficulty, the most important of which are as follows. First, spacecraft in plasmas will experience a net charging effect as they have no connection to ground, called a spacecraft floating potential, ϕ_{sc} (see Appendix A for parameter definitions). That is, spacecraft will have $\phi_{sc} \neq 0$ (e.g., A. L. Besse & A. G. Rubin 1980; H. B. Garrett 1981; J. Geach et al. 2005; V. Génot & S. Schwartz 2004; R. J. L. Grard 1973; R. Grard et al. 1983; S. T. Lai et al. 2017; B. Lavraud & D. E. Larson 2016; A. Pedersen 1995; M. P. Pulupa et al. 2014; C. S. Salem et al. 2001; E. E. Scime et al. 1994; J. D. Scudder et al. 2000; E. C. Whipple 1981). The kinetic energy of incident electrons in the solar wind is much less than ϕ_{sc}, thus ϕ_{sc} affects the energies of measured electrons. Typically spacecraft charge positive in the solar wind owing to the dominance of the photoelectron currents. Thus, all ambient electrons entering a particle detector will have been increased in energy by ϕ_{sc}. Electrons with energies less than ϕ_{sc} are photoelectrons that had insufficient energy to escape the space-

Corresponding author: L.B. Wilson III
Email: lynn.b.wilsoniii@gmail.com

craft. Given that the typical values of ϕ_{sc} ($\sim$7 eV) are comparable to the typical electron temperatures, $T_{e,tot}$ ($\sim$13 eV), correcting the measured energies by ϕ_{sc} is essential for calculating accurate electron velocity moments (e.g., J. Geach et al. 2005; V. Génot & S. Schwartz 2004; B. Lavraud & D. E. Larson 2016; M. P. Pulupa et al. 2014; C. S. Salem et al. 2001; E. E. Scime et al. 1994; P. Song et al. 1997).

The second difficulty is true of all instrumentation, degradation. This challenge is especially true when the instrument is constantly exposed to ionizing radiation, as it is in a space plasma and exposed to sunlight. Thus, it is essential to account for the changes in the detector response as time progresses to ensure that the conversion from raw counts to a physically meaningful unit (e.g., phase space density) is accurate. If the conversion is incorrect, the errors compound when calculating the velocity moments (see Appendix 3 and J. Geach et al. 2005; V. Génot & S. Schwartz 2004; B. Lavraud & D. E. Larson 2016; E. E. Scime et al. 1994; P. Song et al. 1997). Without any clear baseline measurement or "known" values against which to correct the raw measurements, one is left with unknown errors and uncertainties. The best method for providing a "standard candle" measurement against which to calibrate is to derive the total electron density from the upper hybrid line (also called the plasma line) (e.g., see M. M. Martinović et al. 2020; N. Meyer-Vernet & C. Perche 1989). This is the only unambiguous measure of the total electron density one can make with in situ measurements and the uncertainties are only limited to the temporal cadence and frequency resolution of the receiver.

Both of the above issues can be very difficult and time-consuming to properly handle, which is why there are very limited datasets of electron velocity moments in the solar wind[9]. The best available electron velocity moment data from *Wind* were only processed up to 2005 (e.g., C. S. Salem et al. 2023; L. B. Wilson III et al. 2023c) and those data sets had fewer than 850,000 moments[10]. These instruments have a minimum electron energy of measurement, E_{min}, that can be a commandable value changed by instrument teams. The datasets used by C. S. Salem et al. (2023) and L. B. Wilson III et al. (2023c) were calculated when $E_{min} > \phi_{sc}$. Thus, the ϕ_{sc} values served as a free parameter to vary (see Appendix C for further details) until the number density velocity moment matched the known value from quasi-thermal noise (QTN) spectroscopy (e.g., N. Meyer-Vernet & C. Perche 1989; X. Zheng et al. 2026).

Herein we discuss the calibration of the *Wind*/3DP (R. P. Lin et al. 1995; L. B. Wilson III et al. 2021) thermal electron detector, EESA Low (EL), and the generation of velocity moments for all VDFs between January 1, 2005 (i.e., after *Wind* reached L1 and remained there) and November 25, 2017[11]. This time frame is also when $E_{min} < \phi_{sc}$ (e.g., L. B. Wilson III et al. 2023a), a property that is essential to properly calibrate and measure the entire VDF. This paper serves as Paper I in a two-part study. Paper II (L. B. Wilson III et al. 2026) will focus on the statistical analysis of the data.

This paper is outlined as follows: Section 2 introduces the datasets and constraints; Section 3 discusses the methodology for calibrating the detector; and Section 4 discusses and summarizes the calibration and resulting dataset. Paper II will provide scientific analysis of the dataset. Appendices are also included to provide additional details of the parameter definitions (Appendix A), numerical errors/uncertainties in the velocity moments (Appendix B), comparisons to other electron velocity moment datasets (Appendix C), and details about the public dataset (Appendix D).

2. DATA SETS AND METHODOLOGY

All data presented herein were measured by the *Wind* spacecraft (L. B. Wilson III et al. 2021) near 1 au in the solar wind. The thermal electron detector from the 3DP instrument suite (R. P. Lin et al. 1995) is a spherical top-hat, electrostatic analyzer called EESA Low (EL). The data are measured in both burst and survey modes, which have cadences of $\sim$3 seconds and $\sim$24–78 seconds, respectively[12]. The EL data provide a full 4π steradian electron velocity distribution function (VDF) from a few eV[13] to $\sim$1.1 keV. The EL VDFs have 15 energy bins and 88 solid angle look directions with typical resolutions of $\Delta E/E \sim 20\%$ and $\Delta\phi \sim 5°$–$22.5°$, depending on the poloidal anode (i.e., the ecliptic plane bins have higher angular resolution than the zenith). All EL VDFs have

[9] There are useful tables of references in the appendices of L. B. Wilson III et al. (2018) and L. B. Wilson III et al. (2019a) that list several previous works using electron moments in the solar wind.

[10] These data also come from *Wind* but were measured when *Wind* was undergoing multiple perigee passes through the terrestrial magnetosphere (e.g., see Figure 1 in L. B. Wilson III et al. 2021). Thus, the data are not continuous time-wise.

[11] Time range of available quasi-thermal noise analysis data at the time of publication.

[12] All *Wind* 3DP data products discussed herein start from the level zero files found at http://sprg.ssl.berkeley.edu/wind3dp/data/wi/3dp/lz/.

[13] The value of E_{min} is a ground-commandable variable that has changed over time. After January 1, 2005, E_{min} has stayed at $\sim$5 eV except for two short time intervals where it dropped to $\sim$3 eV L. B. Wilson III et al. (e.g., discussed in 2023a).

total integration times defined by the spin period of the spacecraft, which is ∼3 seconds for entire mission. The spacecraft floating potential, ϕ_{sc}, was taken from the dataset described in L. B. Wilson III et al. (2023a).

Quasi-static magnetic field vectors ($\mathbf{B}_o$) were measured by the *Wind*/MFI dual, triaxial fluxgate magnetometers (R. P. Lepping et al. 1995) using the three second cadence data for each particle distribution. Note that the components of some particle moment parameters are defined with respect to $\mathbf{B}_o$ using the subscript j. The parallel(perpendicular) component is defined as $j = \|(\perp)$ and is with respect to $\mathbf{B}_o$.

The upper hybrid frequency, f_{uh}, is determined by tracking the so called "plasma line" or "upper hybrid line" using a neural network algorithm (e.g., see M. M. Martinović et al. 2020) on the *Wind*/WAVES radio data (J.-L. Bougeret et al. 1995) utilizing quasi-thermal noise (QTN) spectroscopy (e.g., N. Meyer-Vernet & C. Perche 1989). Specifically, the data come from the thermal noise receiver (TNR), which has up to a ∼4 second cadence and a frequency resolution of ∼4.3%. We specifically use the filtered QTN data from NASA's Space Physics Data Facility (SPDF)[14].

The proton velocity moments were taken from the *Wind*/SWE Faraday Cups (FCs) (K. W. Ogilvie et al. 1995). The SWE nonlinear least-squares fit (J. C. Kasper et al. 2006) have a ∼92 second cadence covering an energy-per-charge range of ∼150–8000 eV/C with a variable energy(speed) resolution of ∼6.5–13%(∼3.3–6.5%), depending on energy window.

There were 3,996,051 electron VDFs examined in this study. We interpolate the SWE, WAVES, and MFI data to the VDF midpoint times. We found 3,947,607 VDFs had finite velocity moments that satisfied the following constraints/criteria (see Appendix A for parameter definitions):

$V_{oe,x} < 0$ km/s;
$|q_{e,\|}|/q_{eo} < 1$;
$T_{e,j} \geq 1$ eV;
3 eV $\leq \phi_{sc} \leq$ 30 eV; and
$n_{e,int} \geq n_{min}$.

The above criteria are defined for physically meaningful reasons. The requirement that $V_{oe,x} < 0$ km/s is just that the bulk of the electrons should not flow toward the Sun in the spacecraft frame. We also know that $|q_{e,\|}|/q_{eo}$ < 1 should be satisfied given that a value ≥1 would imply the entire VDF is drifting away from the Sun (i.e., all electrons would be heat flux-carrying particles). The $T_{e,j} \geq 1$ eV comes about because the instrument lacks

[14] https://spdf.gsfc.nasa.gov

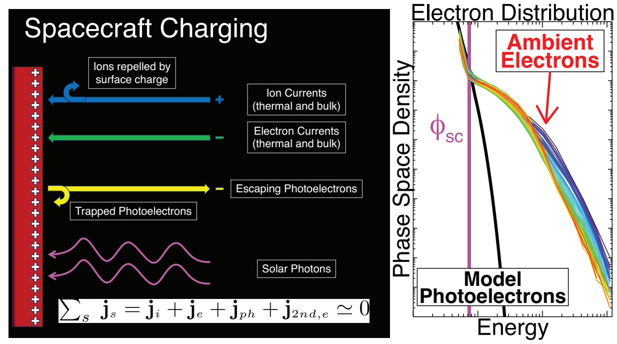

Figure 1. Left: A cartoon illustrating the currents responsible for spacecraft charging. **Right:** An example *Wind* EL electron VDF showing both photoelectrons and ambient electrons. The solid black line shows a Maxwellian which well models the photoelectrons (adapted from Figure 1 in L. B. Wilson III et al. 2023a). The spacecraft potential is not determined from a modeled Maxwellian, however.

the energy resolution to measure $T_{e,j} < 1$ eV. The 3 eV $\leq \phi_{sc} \leq$ 30 eV requirement derives from the ϕ_{sc}, which has no valid values outside this range (L. B. Wilson III et al. 2023a). Finally, $n_{e,int} \lesssim n_{min}$ values were ignored because the instrument cannot measure such small densities and if the density is truly smaller than n_{min} then that VDF could not be calibrated (see Section 3.2).

The 3,947,607 finite velocity moments differ from the 3,996,051 VDFs by 48,444 because these are the number of pre-existing, long-duration[15] data gaps in some of the original data products. This approach was used to reduce numerical artifacts introduced by interpolation over large gaps in the WAVES and SWE data.

Thus, from the 3,996,051 VDFs examined herein, there were 3,947,607 finite velocity moments and 625 non-finite velocity moments.

3. CALIBRATION METHOD

In this section, we outline the measurement techniques and methods necessary to calibrate the 3DP EL detector. This step is necessary because of changes in the detector efficiency for each anode due to degradation and changes in instrument operational modes (e.g., F. Bordoni 1971; C. W. Carlson et al. 1982; C. W. Carlson & J. P. McFadden 1998; G. A. Collinson & D. O. Kataria 2010; R. R. Goruganthu & W. G. Wilson 1984; J. D. Mackenzie 1977; B. R. Sandel et al. 1977; J. L. Wiza 1979). It should also be noted that the spacecraft potential, ϕ_{sc}, can and does affect the calibration as we discuss below.

[15] These are defined as 20 adjacent solutions all having invalid velocity moments.

3.1. *Spacecraft Potential*

In this section, we discuss how we determine the spacecraft floating potential, ϕ_{sc}, from the electron VDFs.

Spacecraft in plasmas will experience a net charging effect as they have no connection to ground, corresponding to $\phi_{sc} \neq 0$ (e.g., A. L. Besse & A. G. Rubin 1980; M. F. Diaz-Aguado et al. 2021; H. B. Garrett 1981; J. Geach et al. 2005; V. Génot & S. Schwartz 2004; R. J. L. Grard 1973; R. Grard et al. 1983; S. T. Lai et al. 2017; B. Lavraud & D. E. Larson 2016; A. Pedersen 1995; M. P. Pulupa et al. 2014; C. S. Salem et al. 2001; E. E. Scime et al. 1994; J. D. Scudder et al. 2000; E. C. Whipple 1981). The current sources causing a non-zero ϕ_{sc} are thermal and bulk flow currents from the ambient plasma, photoelectron currents, and impact ionization currents (see Figure 1, left panel, for an illustration). On average[16], spacecraft with conductive surface materials in the solar wind and in sunlight will have $\phi_{sc} > 0$.

One can measure ϕ_{sc} using particle VDFs or DC-coupled electric field data. Unfortunately *Wind* does not have DC-coupled electric field data. However, when $E_{min} < \phi_{sc}$ is satisfied, one can determine ϕ_{sc} from electron VDFs. This effect is because any ambient electron measured inside the detector will gain an energy equal to the potential caused by ϕ_{sc}. That is, all electron energies measured in the instrument frame of reference are larger than their energies at infinity by ϕ_{sc}.

When $E_{min} < \phi_{sc}$, the instrument will also measure photoelectrons that were not energetic enough to escape, and were thus recaptured by the spacecraft. These photoelectrons contaminate the data[17] and appear as a large "spike" or abrupt enhancement at low energies in electron VDF measurements. It is that abrupt enhancement that serves as the feature used to determine ϕ_{sc} for this study (i.e., dataset described by L. B. Wilson III et al. 2023a). The dataset herein only uses VDFs from time periods when $E_{min} < \phi_{sc}$ was satisfied.

Figure 1 (right panel) shows an example electron VDF observed by the *Wind* 3DP EL detector. The VDF is plotted in phase space density versus measured energy in the instrument frame of reference (i.e., the energy bins have not been adjusted for ϕ_{sc}). The 88 color-coded curves correspond to all the solid angle bins of the EL detector. The solid black curve shows a model fit to the photoelectron population and the solid magenta line marks the approximate location of ϕ_{sc} for this VDF (i.e., from L. B. Wilson III et al. 2023a).

The accuracy of ϕ_{sc} derived from the approach used by L. B. Wilson III et al. (2023a) is entirely dependent upon the energy bin width of the bin in which ϕ_{sc} falls. That is, the *Wind* 3DP EL detector has logarithmically-spaced energy bins so as the energy bin number increases, ΔE inceases logarithmically. Thus, as ϕ_{sc} increases, the uncertainty in ϕ_{sc} increases nonlinearly. We discuss this issue in detail in Appendix B.

3.2. *The Plasma Line*

In this section, we discuss how we determine the total electron number density so we have a value against which to calibrate the particle instrument.

Figure 2 shows the magnetic field magnitude, its components, and the dynamic radio spectra for roughly a week of January 2013. The magenta line on the bottom panel shows our automated estimate of f_{uh} (shifted vertically to lower frequencies so the reader can see the f_{uh} emission) (e.g., see M. M. Martinović et al. 2020). The technique is called quasi-thermal noise (QTN) spectroscopy (e.g., N. Meyer-Vernet & C. Perche 1989; X. Zheng et al. 2026). We have also labeled a few Type III solar radio bursts just for reference. This interval illustrates our ability to accurately and automatically find f_{uh} from the data.

We know that $n_{e,WAVES} \propto f_{pe}{}^2$ and that $f_{uh} \sim f_{pe}$ (i.e., the difference between these two frequencies is less than 1% under typical solar wind conditions[18]) (e.g., L. B. Wilson III et al. 2021). The algorithm that finds f_{uh} actually determines the value at the half-frequency bin level, thus the $n_{e,WAVES}$ values derived from f_{uh} are accurate to ∼4% (e.g., see M. M. Martinović et al. 2020). Thus, the absolute lowest possible uncertainty of any $n_{e,int}$ value in this dataset will be ∼4%. However, due to the discreteness of the energy bins of the detector and the method used to find ϕ_{sc} (e.g., again see Appendix B), the actual uncertainty[19] of most $n_{e,int}$ values will exceed 10%.

The filtered QTN data used herein has a median cadence of one f_{uh} every ∼4 seconds. Although 3DP in burst mode measures a full 3D VDF every ∼3 seconds,

[16] Typically, one assumes that these currents balance such that ϕ_{sc} varies slowly, which is true except in large amplitude fluctuating electric fields (e.g., M. H. Boehm et al. 1994). However, for the sake of the current work, these fluctuations will be averaged out for our comparatively low cadence data.

[17] The photoelectron population outnumbers the ambient plasma electrons by more than an order of magnitude (e.g., R. J. L. Grard 1973; R. Grard et al. 1983).

[18] Even though the electron cyclotron frequency, f_{ce}, contributes very little to f_{uh}, we still account for it when calculating f_{pe}.

[19] This is not a statement about statistical uncertainties but that of systematic because the statistical uncertainties are almost always much smaller. As we state above, the $n_{e,WAVES}$ values can be accurate to ∼4%. In contrast, ϕ_{sc} is never more accurate than 10%, which directly affects the resultant $n_{e,int}$.

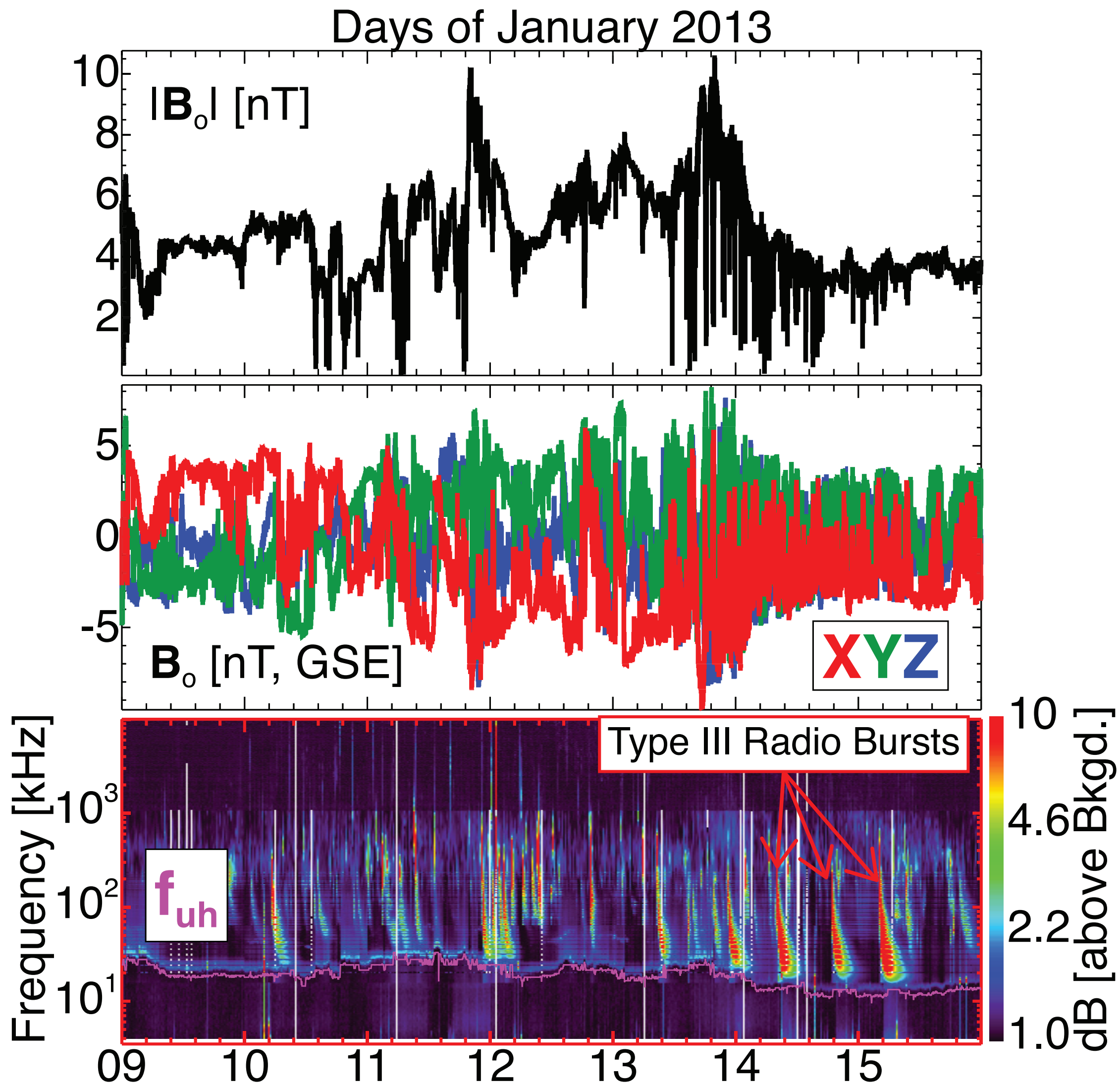

Figure 2. Example showing our ability to automatically find f_{uh} during January 2013. The plot shows, from top-to-bottom, B_o [nT]; GSE components of $\mathbf{B}_o$ [nT]; and the WAVES radio dynamic spectra data [dB above background]. A few Type III radio bursts are labeled for reference. The magenta line in the last panel, marking f_{uh}, has been vertically shifted so the reader can observe the WAVES feature known as the plasma line.

the majority of the VDFs are ~24–97 seconds apart depending upon the instrument mode. In the time range relevant to this study, there are 17,681,098 TNR time stamps, of which 9,380,158 have finite f_{uh} solutions. Of those 9,380,158 finite f_{uh} solutions, 8,336,226(47.15%) corresponded to $n_{e,WAVES} \geq 4$ cm^{-3} (the significance of this value is discussed in Section 3.3 below). The $n_{e,WAVES}$ have been interpolated to the 3DP times as discussed in Section 2.

As previously stated, the f_{uh} values are found using an automated neural network. The upper hybrid emission is not the most intense signal in the radio data. In fact, it is often one of the weakest signals compared to ion-acoustic wave noise and solar radio bursts (e.g., M. M. Martinović et al. 2020; L. B. Wilson III et al. 2007). Consequently, f_{uh} values can have several data gaps due to incorrect identification. During some of these intervals, we cannot determine corrections for the 3DP data as we have no $n_{e,WAVES}$ baseline values against which to calibrate. Thus, of the 3,996,051 total VDFs examined herein, we have 3,947,607 VDFs with valid calibrations.

3.3. *Anode Efficiency Corrections*

In this section, we discuss how we calculate the efficiency corrections for each of the eight EESA Low (EL) anodes that are applied like corrections to the detector geometric factor in the unit conversion software (see Equations B2a–B2c in Appendix B).

The EL optical geometric factor is $\mathbf{GF}_{opt} = 0.0126$ cm^2 sr, which was determined from ray tracing simulations and testing pre-launch. EL has eight anodes, each assigned a correction to this optical geometric factor (e.g., see instrument description in R. P. Lin et al. 1995). The original anode-specifc corrections were determined after launch and are given as (e.g., see description in public 3DP software in L. B. Wilson III 2021):

$\mathbf{GF}_{def} = [0.977, 1.019, 0.990, 1.125, 1.154, 0.998, 0.977, 1.005]$. The values were determined to ensure that electron VDFs remain gyrotropic[20] regardless of ϕ_{sc}, which largely remains true to the present day. Thus, the corrections to $\mathbf{GF}_{def}$, called $\mathbf{GF}_{cor}$, are uniform increases or decreases in all eight values for this dataset. These changes are done in order to match the integrated number density to the one determined from the WAVES measurements.

A more typical and less time-intensive approach involves determining a mean or median value for the time-varying $\mathbf{GF}_{cor}$ with updates on a cadence of months to years (e.g., as is done for the THEMIS ESAs J. P. McFadden et al. 2008b,a), depending on the instrument/mission. This approach is more easily done on missions that can directly measure ϕ_{sc} using DC-coupled electric field probes, such as THEMIS (e.g., J. W. Bonnell et al. 2008). *Wind* does not have a continuous, DC-coupled electric field measurement, so we are left with the discrete solutions derived from features in the electron VDFs (i.e., L. B. Wilson III et al. 2023a). The magnitude of the difference between the true ϕ_{sc} and the one derived from the electron VDFs depends on the energy bin width near the ϕ_{sc} solution. The energy bins for the 3DP EL detector are logarithmically spaced, so the larger ϕ_{sc} intervals also have larger uncertainties in ϕ_{sc} (see Section 3.1 for more details). This uncertainty precludes our ability to generate longer term averages for $\mathbf{GF}_{cor}$, and we must rely upon new values for $\mathbf{GF}_{cor}$ for each VDF[21]. Thus, $\mathbf{GF}_{cor}$ serves as both a correction to $\mathbf{GF}_{def}$ and ϕ_{sc}.

The steps to calibrate any given electron VDF (see also Appendix B for more details) are as follows:

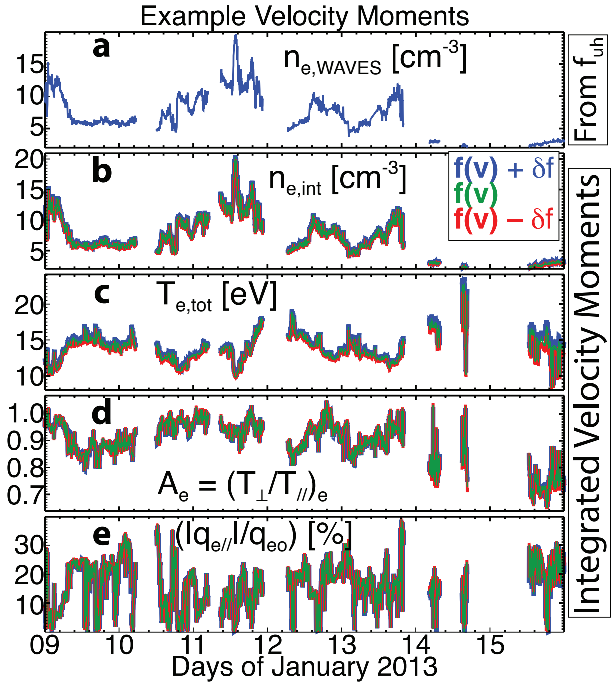

Figure 3. Calibrated electron velocity moments for the same time period as shown in Figure 2. The panels are as follows: **a** shows $n_{e,WAVES}$ (derived from f_{uh}) [cm^{-3}]; **b** shows the zeroth velocity moment, $n_{e,int}$ [cm^{-3}]; **c** shows the total electron temperature, $T_{e,tot}$ [eV]; **d** shows the electron temperature anisotropy, A_e [N/A]; and **e** shows the signed, normalized parallel electron heat flux, $\frac{|q_{e,\parallel}|}{q_{eo}}$ [%]. The last panel is shown as a percentage rather than fraction, where $\frac{|q_{e,\parallel}|}{q_{eo}} = 0\%$ means no parallel heat flux. The heat flux is normalized to the free streaming limit (e.g., S. P. Gary et al. 1999) defined in Equation A1j.

Calibration Measurements

(a) determine ϕ_{sc} from the particle VDF[22]

(b) determine the upper hybrid frequency, f_{uh}, from the WAVES radio data[23]

(c) invert[24] f_{uh} to determine f_{pe}, from which we can calculate the total electron density, $n_{e,WAVES}$ (e.g., see Equation A1i in Appendix A)

Calibration Process

(a) for each VDF, $f(\mathbf{v})$, correct the energies for ϕ_{sc}

[20] Although it is often assumed that spacecraft have a spherically symmetric ϕ_{sc} monopolar scalar field, this is not true. There are measureable dipole corrections (e.g., M. P. Pulupa et al. 2014) and asymmetries due to the spacecraft geometry, different surface materials, etc. (e.g., E. E. Scime et al. 1994). All corrections herein assume a spherically symmetric, monopolar scalar electric potential as these deviations have been shown to be small.

[21] We iteratively change $\mathbf{GF}_{cor}$ by no more than 10% for each iteration and allow for no more than 30 iterations. If a solution is not reached within those 30 iterations, the $\mathbf{GF}_{cor}$ is defined as NaNs and that VDF is ignored. These criteria were determined empirically.

[22] The values of ϕ_{sc} were taken from database described by L. B. Wilson III et al. (2023a).

[23] The values of f_{uh} were taken from database described by M. M. Martinović et al. (2020).

[24] We do account for f_{ce} in the the inversion to find the electron density.

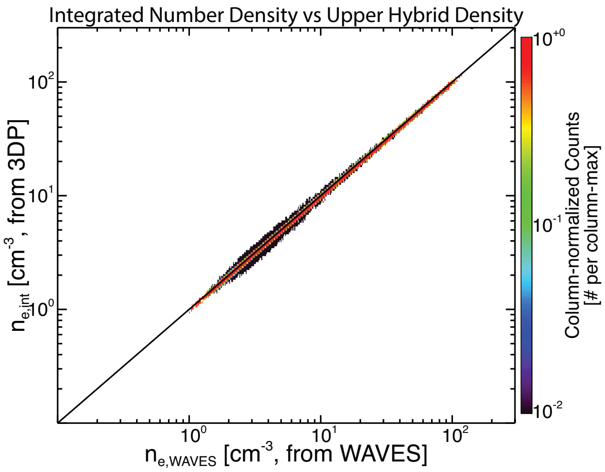

Figure 4. A 2D column-normalized histogram of $n_{e,int}$ [cm^{-3}] versus $n_{e,WAVES}$ [cm^{-3}]. The columns are normalized by the maximum number of counts of all the histogram bins in that column. The diagonal black line shows when $n_{e,int} = n_{e,WAVES}$. Only data with Quality Flag ≤ 7 are shown (see Appendix D for definitions).

  (b) numerically integrate[25] $f(\mathbf{v})$ to calculate a number density, $n_{e,int}$
  (c) adjust $\mathbf{GF}_{cor}$ accordingly so that $n_{e,int}$ will move closer to $n_{e,WAVES}$
  (d) re-integrate $f(\mathbf{v})$ to get a new $n_{e,int}$ and adjust $\mathbf{GF}_{cor}$
  (e) repeat as necessary until $\zeta \equiv |n_{e,int} - n_{e,WAVES}|/n_{e,WAVES} \times 100\% \leq$ some user-defined threshold (see discussion below and Appendix B)

Calibrated Velocity Moments

  (a) apply the converged $\mathbf{GF}_{cor}$ to each VDF[26]
  (b) create two copies of each VDF and redefine the data such that:
    i. we add or subtract the Poisson counting statistics from the original to get three solutions for each VDF: $f(\mathbf{v}) - \delta f(\mathbf{v})$, $f(\mathbf{v})$, and $f(\mathbf{v}) + \delta f(\mathbf{v})$
    ii. convert each to phase space density
  (c) numerically integrate $f(\mathbf{v}) - \delta f(\mathbf{v})$, $f(\mathbf{v})$, and $f(\mathbf{v}) + \delta f(\mathbf{v})$ up to third velocity moment (i.e., heat flux)
  (d) the velocity moments of $f(\mathbf{v}) - \delta f(\mathbf{v})$ and $f(\mathbf{v}) + \delta f(\mathbf{v})$ serve as the worst case statistical uncertainties of $f(\mathbf{v})$
  (e) example computions are shown in Figure 3

Figure 3 shows velocity moments $n_{e,int}$ through $q_{e,\|}/q_{eo}$ that were calculated after we applied $\mathbf{GF}_{cor}$ for each VDF. Panel **a** shows $n_{e,WAVES}$ (determined from f_{uh} shown in Figure 2) and Panels **b–e** are numerically integrated velocity moments of the EL electron VDFs. The color-coded lines illustrate the worst possible statistical errors[27]. These are calculated by adding (blue lines, $f(\mathbf{v}) + \delta f(\mathbf{v})$) and subtracting (red lines, $f(\mathbf{v}) - \delta f(\mathbf{v})$) the Poisson statistics from the the original VDF (green lines, $f(\mathbf{v})$) when in units of counts. The resulting dataset (see Appendix D for more details) from our includes these Poisson uncertainties as a baseline error estimate. These data in Figure 3 are all consistent with typical solar wind values (e.g., C. S. Salem et al. 2023; L. B. Wilson III et al. 2019a, 2023c).

Ideally, one would want ζ, introduced above, to be zero, but that is nearly impossible numerically. In fact, benchmark testing shows that reducing the value below $\sim$6.5% causes the run time for each VDF calibration to increase exponentially with decreasing threshold percentages. Thus, we use $\zeta \leq 6.5\%$ as the threshold percent difference. This choice means that the difference between $n_{e,int}$ and $n_{e,WAVES}$ should be $\leq 7\%$ (see Appendix B for additional complications), which is comparable to or smaller than the usual uncertainties for velocity moments from these types of instruments (e.g., see P. Song et al. 1997; L. B. Wilson III et al. 2022). The higher order velocity moments will have larger uncertainties, but this is normal and usually results from compounding uncertainties due to lower order moment inaccuracies.

Even though the uncertainties computed from perturbing the Poisson counting statistics are the worst-case statistical uncertainties (e.g., see D. J. Gershman et al. 2015; R. J. Wilson 2015, for analytical statistical uncertainty estimates), they are smaller than the actual, systematic uncertainties (e.g., see discussions in A. Cara et al. 2017; J. De Keyser et al. 2018; R. De Marco et al. 2016; P. Song et al. 1997; S. J. Schwartz et al. 2022; L. B. Wilson III et al. 2022). Further, more recent work has shown that the previously held assumption of constant gain from a microchannel plate (MCP) above a threshold incident particle energy[28] is not cor-

[25] All numerical integrals used a 3D Simpson's 1/3 Rule with a uniform velocity grid constructed with 3D Delaunay tetrahedralization (e.g., see L. B. Wilson III et al. 2019a, 2022).

[26] The correction must be applied while the data are still in units of counts as the conversion to phase space density depends nonlinearly upon $\mathbf{GF}_{cor}$.

[27] The total systematic errors will be larger than these because 3DP has good counting statistics in the solar wind. For VDF measurements with low counting statistics or low signal-to-noise ratios, these statistical errors are proportionally much larger.

[28] Early work on MCPs suggested that above some incident threshold energy, the resultant shower of electrons emitted onto the exit anode would be roughly constant with increasing energy (e.g., B. Brehm et al. 1995). This scenario was mostly

rect (e.g., D. J. Gershman et al. 2016). Unfortunately, we do not have access to ground test results as *Wind* is now over 31 years old and such records are not digitally stored/archived. Therefore, we are left to use the above algorithm as the best we can do.

Figure 4 shows a 2D column-normalized histogram of $n_{e,int}$ versus $n_{e,WAVES}$ to illustrate where the velocity moments can and cannot be trusted. Only data with Quality Flag ≤ 7 are shown (see Appendix D for definitions). The data are consistent with previous efforts to calibrate *Wind*/3DP, but those efforts considered much shorter time periods of data (e.g., C. S. Salem et al. 2001, 2023; L. B. Wilson III et al. 2019b). Note that the detector has an ideal operational range of electron densities that falls between $\sim$4 cm^{-3} and $\sim$90 cm^{-3}.

Notice that in Figure 4 as $n_{e,WAVES}$ goes below $\sim$7 cm^{-3} the spread in the solutions increase. Even so, there is very good agreement between the numerically integrated VDFs and the QTN number densities.

Since *Wind* cannot directly measure ϕ_{sc}, the accuracy of our ϕ_{sc} estimates depend upon the resolution of the particle detector energy bins (discussed in Section 3.1 and in Appendix B). The *Wind*/3DP detectors have logarithmically spaced energy bins with a nearly constant $\Delta E/E$. However, this means that as ϕ_{sc} increases, it falls in ever larger ΔE bins. Thus, as the real ϕ_{sc} increases, the uncertainty of our estimated ϕ_{sc} increases exponentially. Even without this complication, the EL detector has an ideal operational range of electron densities that falls between $\sim$4 cm^{-3} and $\sim$90 cm^{-3}. It can measure densities above or below this range, but the uncertainties increase.

4. SUMMARY AND DISCUSSION

We have calibrated 3,996,051 electron VDFs observed by the *Wind*/3DP EESA Low detector between January 1, 2005 and November 25, 2017. The SWE and WAVES data were interpolated to the midpoint times of the 3DP VDFs. The solutions are assigned an associated quality flag (see Appendix D for definitions) for the user's benefit and guidance.

This dataset represents the first long-duration (i.e., $\geq$12.5 years), properly calibrated electron velocity moment dataset in the near-Earth solar wind. The dataset will be publicly available and archived at NASA's Space Physics Data Facility (SPDF)[29]. Electrons represent a critical missing piece in our attempt to understand the heating and acceleration of the solar wind. In Paper II, we present some preliminary analysis of the dataset. Future work will involve extending the dataset to the present as more measurements of f_{uh} become available.

ACKNOWLEDGMENTS

Analysis software[30] (L. B. Wilson III 2021) and *Wind*/3DP level zero data files[31] used herein are publicly available. The *Wind* spacecraft floating potential measurements are found at L. B. Wilson III et al. (2023b). The WAVES upper hybrid line data are found at M. M. Martinović et al. (2020). The electron velocity moments generated for this work are publicly available through NASA's Space Physics Data Facility (SPDF)[32]. JMT was supported by NASA grant 80NSSC23K0099. KGK and MMM were supported by NASA grant 80NSSC22K101. SDB is supported in part by a UK Royal Society Wolfson Visiting Fellowship.

APPENDIX

A. DEFINITIONS

In this appendix, the symbols and notation used throughout this manuscript are defined. All direction-dependent parameters use the subscript j to represent the direction, where $j = tot$ for the entire distribution, $j = \parallel$ for the parallel direction, and $j = \perp$ for the perpendicular direction, where parallel/perpendicular is with respect to the quasi-static magnetic field vector, $\mathbf{B}_o$ [nT]. Below are the symbol/parameters definitions:

acronyms, initialisms, and symbols

− VDF ≡ velocity distribution function

tested with ions being the incident particles. When electrons are the incident particle, the gain is not constant with increasing energy (e.g., R. R. Goruganthu & W. G. Wilson 1984), but it was not thought to be as variable as recent work shows.

[29] https://spdf.gsfc.nasa.gov

[30] https://github.com/lynnbwilsoniii/wind_3dp_pros

[31] http://sprg.ssl.berkeley.edu/wind3dp/data/wi/3dp/lz/

[32] https://spdf.gsfc.nasa.gov

- 3DP ≡ A Three-Dimensional Plasma and Energetic Particle Investigation for the Wind Spacecraft (i.e., instrument paper R. P. Lin et al. 1995)
- GSE ≡ Geocentric Solar Ecliptic cartesian coordinate basis (e.g., M. Fränz & D. Harper 2002)
- FAC ≡ field-aligned coordinates, where the components are either (parallel, perpendicular, total) or (perpendicular 1, perpendicular 2, parallel)

one-variable statistics

- X_{min} ≡ minimum
- X_{max} ≡ maximum
- $\bar{X}$ ≡ mean
- $\tilde{X}$ ≡ median
- $X_{25\%}$ ≡ lower quartile
- $X_{75\%}$ ≡ upper quartile
- $X_{y\%}$ ≡ yth percentile
- σ ≡ standard deviation
- σ^2 ≡ variance

fundamental parameters

- ε_o ≡ permittivity of free space [F m^{-1}]
- μ_o ≡ permeability of free space [H m^{-1}]
- c ≡ speed of light in vacuum [km s^{-1}] = $(\varepsilon_o\ \mu_o)^{-1/2}$
- k_B ≡ the Boltzmann constant [J K^{-1}]
- e ≡ the fundamental charge [C]

plasma parameters

- n_s ≡ the number density [cm^{-3}] of species s
- m_s ≡ the mass [kg] of species s
- Z_s ≡ the charge state of species s
- q_s ≡ the charge [C] of species $s = Z_s\ e$
- $T_{s,j}$ ≡ the scalar temperature [eV] of the jth component of species s
- $V_{Ts,j}$ ≡ the most probable thermal speed [km s^{-1}] of a one-dimensional velocity distribution (see Equation A1b)
- $\mathbf{V}_{os}$ ≡ the drift velocity [km s^{-1}] of species s in the plasma relative to a specified rest frame
- $\mathbf{V}_{sw}$ ≡ bulk flow velocity [km s^{-1}] of the solar wind in the spacecraft frame of reference
- $P_{Ts} = n_s\ k_B\ T_{s,tot}$ ≡ scalar total thermal pressure [eV cm^{-3}] of species s
- $A_s = \frac{T_{s,\perp}}{T_{s,\parallel}}$ ≡ temperature anisotropy [N/A] of species s
- ϕ_{sc} ≡ the scalar, quasi-static spacecraft potential [eV] (e.g., M. P. Pulupa et al. 2014; E. E. Scime et al. 1994)
- Ω_{cs} ≡ the angular cyclotron frequency [rad s^{-1}] (see Equation A1c)
- ω_{ps} ≡ the angular plasma frequency [rad s^{-1}] (see Equation A1d)
- λ_{De} ≡ the electron Debye length [m] (see Equation A1e)
- ρ_{cs} ≡ the thermal gyroradius [km] (see Equation A1f)
- λ_s ≡ the inertial length [km] (see Equation A1g)
- $\beta_{s,j}$ ≡ the plasma beta [N/A] of the jth component of species s (see Equation A1h)
- ω_{uh} ≡ the angular upper hybrid resonance frequency [rad s^{-1}] (see Equation A1i)
- $n_{e,WAVES}$ ≡ the total electron number density [cm^{-3}] derived from the upper hybrid line measured by the WAVES radio detectors
- $n_{e,int}$ ≡ the zeroth velocity moment of an electron VDF[33], i.e., the total electron number density [cm^{-3}]
- $\mathbf{q}_e$ ≡ the electron heat flux 3-vector [μW m^{-2}] derived from the third velocity moment of an electron VDF (sometimes referred to as the skewness of a distribution)
- $q_{e,\parallel}$ ≡ the parallel (with respect to $\mathbf{B}_o$) projection of $\mathbf{q}_e$ [μW m^{-2}], also called the parallel electron heat flux
- q_{eo} ≡ free streaming heat flux limit [μW m^{-2}] (see Equation A1j)

[33] All velocity moments are calculated using a Simpson's $\frac{1}{3}$ Rule algorithm for the numerical integration (e.g., see L. B. Wilson III et al. 2019a, 2022). There are no nonlinear fits done to determine electron moments from the 3DP data herein.

- $\zeta = 6.5\% \equiv$ absolute value of the percent difference between $n_{e,int}$ and $n_{e,WAVES}$ (see Equation A1k)
- $f(\mathbf{v}) \equiv$ three-dimensional velocity distribution function (VDF) [# cm^{-3} km^{-3} s^{+3}]
- $\delta f(\mathbf{v}) \equiv$ Poisson uncertainty of $f(\mathbf{v})$ [# cm^{-3} km^{-3} s^{+3}], calculated by taking the square-root of $f(\mathbf{v})$ while in units of counts then converting to phase space density

instrument parameters

- $\mathbf{GF}_{opt} = 0.0126$ cm^2 sr $\equiv$ The optical geometric factor of the 3DP EESA Low thermal electron detector
- $\mathbf{GF}_{def} \equiv$ The default anode-by-anode correction to $\mathbf{GF}_{opt}$
- $\mathbf{GF}_{cor} \equiv$ The VDF-specific, anode-by-anode correction to $\mathbf{GF}_{opt}$, i.e., the correction to $\mathbf{GF}_{def}$ for each VDF
- $\phi_{sc} \equiv$ spacecraft floating electric potential [eV]
- $E_{min} \equiv$ the minimum energy bin midpoint value [eV] of a particle detector
- $n_{min} \equiv$ the minimum number density [cm^{-3}] one can resolve with the *Wind*/WAVES radio data ($\sim$0.2 cm^{-3}) due to the lowest frequency of the TNR instrument
- $\tau_d \equiv$ the anode-specific deadtime (e.g., see F. Bordoni 1971; R. R. Goruganthu & W. G. Wilson 1984) [s] which varies from 1.5×10^{-7} s to 6×10^{-7} s for *Wind* 3DP EL
- $\delta t \equiv$ the accumulation time [s] each energy-angle bin (on the order of 10s to 100s of milliseconds for each energy-angle bin)
- $E_j \equiv$ the mid-point energy of the jth energy bin [eV]
- $m_{e,3DP} \equiv$ the electron mass in units of electron volts per speed of light squared, but c is in units of km/s $\sim 5.68563\times10^{-6}$ eV km^{-2} s^{+2}
- $\mathcal{R}_c \equiv$ raw count rates [# s^{-1}] (see Equation B2a)
- $\mathcal{R}_s \equiv$ scaled count rates [N/A] (see Equation B2b)
- $\mathcal{F} \equiv$ conversion factor from raw counts to phase space density for each energy-angle bin [e.g., # cm^{-3} km^{-3} s^{+3} sr^{-1}] (see Equation B2c)

The variables that rely on multiple parameters are given in the following equations:

$$T_{s,tot} = \frac{1}{3}\left(T_{s,\parallel} + 2\ T_{s,\perp}\right) \tag{A1a}$$

$$V_{Ts,j} = \sqrt{\frac{2\ k_B\ T_{s,j}}{m_s}} \tag{A1b}$$

$$\Omega_{cs} = \frac{q_s\ B_o}{m_s} \tag{A1c}$$

$$\omega_{ps} = \sqrt{\frac{n_s\ {q_s}^2}{\varepsilon_o\ m_s}} \tag{A1d}$$

$$\lambda_{De} = \frac{V_{Te,tot}}{\sqrt{2}\ \omega_{pe}} = \sqrt{\frac{\varepsilon_o\ k_B\ T_{e,tot}}{n_e\ e^2}} \tag{A1e}$$

$$\rho_{cs} = \frac{V_{Ts,tot}}{\Omega_{cs}} \tag{A1f}$$

$$\lambda_s = \frac{c}{\omega_{ps}} \tag{A1g}$$

$$\beta_{s,j} = \frac{2\mu_o n_s k_B T_{s,j}}{|\mathbf{B}_o|^2} \tag{A1h}$$

$${\omega_{uh}}^2 = {\omega_{pe}}^2 + {\Omega_{ce}}^2 \tag{A1i}$$

$$q_{eo} = \frac{3}{2\sqrt{2}} m_e\ n_e\ {V_{Te}}^3 \tag{A1j}$$

$$\zeta = \frac{|n_{e,int} - n_{e,WAVES}|}{n_{e,WAVES}} \times 100\% \tag{A1k}$$

B. SOURCES OF ERROR

In this appendix, we discuss the complication of relying upon the discrete ϕ_{sc} values derived by L. B. Wilson III et al. (2023a) as mentioned in Sections 3.1 and 3.3.

First we must define how we convert from raw counts to phase space density. The parameters on which the conversion factor (e.g., see F. Bordoni 1971; C. W. Carlson et al. 1982; C. W. Carlson & J. P. McFadden 1998; G. A. Collinson & D. O. Kataria 2010; R. R. Goruganthu & W. G. Wilson 1984; J. D. Mackenzie 1977; B. R. Sandel et al. 1977; J. L. Wiza 1979), $\mathcal{F}$, depends are: deadtime τ_{d} [s], accumulation time δt [s], counts $\mathcal{C}$ [#], the anode corrections $\mathbf{GF}_{cor}$, the optical goemetric factor $\mathbf{GF}_{opt}$, the mid-point energy of the jth energy bin E_{j} [eV], and the electron mass $m_{e,3DP}$ [eV km^{-2} s^{+2}]. The equations to convert from raw counts to phase space density [e.g., # cm^{-3} km^{-3} s^{+3}] are:

$$\mathcal{R}_{c} = \frac{\mathcal{C}}{\delta t} \tag{B2a}$$

$$\mathcal{R}_{s} = 1 - \mathcal{R}_{c}\ \tau_{d} \tag{B2b}$$

$$\mathcal{F} = \frac{1}{\mathcal{R}_{s}\left[\delta t\ \mathbf{GF}_{opt}\ \mathbf{GF}_{cor}\ {E_{j}}^{2}\ \left(2 \times 10^{5}\ {m_{e,3DP}}^{-2}\right)\right]} \tag{B2c}$$

The factor of 2×10^{5} is a two-part conversion. The two comes from the nonrelativistic kinetic energy (i.e., 2E/m) and the 10^{5} is converting kilometers to centimeters. Thus, the units of $\mathcal{F}$ for the *Wind* 3DP EL detector are # cm^{-3} km^{-3} s^{+3}.

For each VDF, we numerically integrate $f\left(\mathbf{v}\right)$ to find the zeroth velocity moment, $n_{e,int}$. We calculate the percent difference between this value and that from the upper hybrid line, $\zeta = \lvert n_{e,int} - n_{e,WAVES} \rvert / n_{e,WAVES} \times 100\%$. If $\zeta \leq 6.5\%$, then the value of $n_{e,int}$ is kept and $\mathbf{GF}_{cor}$ is defined. If $\zeta > 6.5\%$, then we increase(decrease) $\mathbf{GF}_{cor}$ by 10% if $n_{e,int}$ is greater(less) than $n_{e,WAVES}$. This is done iteratively until $\zeta \leq 6.5\%$. If this does not happen within 30 iterations, the VDF is not calibrated and that $\mathbf{GF}_{cor}$ is set to NaNs and the routine moves on to the next VDF. We limited the iterations because after 30 the difference between $\mathbf{GF}_{cor}$ and $\mathbf{GF}_{def}$ becomes unrealistically large. We also limited the iterations to improve computational efficiency because we found some VDFs going through 1000s of iterations without ever converging to $\zeta \leq 6.5\%$ (i.e., $n_{e,int}$ would bounce around $n_{e,WAVES}$ but always stay far enough away to preclude convergence)[34].

Given the large number of VDFs examined herein, the most time-effective approach was to determine $\mathbf{GF}_{cor}$ for all valid VDFs in the given time range first. That is, we went through all VDFs and determined $\mathbf{GF}_{cor}$ for each one if $\zeta \leq 6.5\%$ was achieved. This gave us a list of $\mathbf{GF}_{cor}$ values. Then we applied these $\mathbf{GF}_{cor}$ values to all the VDFs and numerically integrated the VDFs to calculate the velocity moments for any with valid $\mathbf{GF}_{cor}$ values[35]. This two-step approach is much more feasible, computationally and time-wise, than finding $\mathbf{GF}_{cor}$ and then immediately computing the velocity moments before iterating to the next VDF[36]. We used two computers (a 2023 MacBook Pro with Apple M2 Max and a 2025 Mac Studio with Apple M3 Ultra) to reduce the human time commitment[37], but it still required >5 weeks (∼8-10 hour days, 5 days a week) to calibrate and integrate the 3,996,051 VDFs in the dataset.

During the numerical integration, we performed a 3D Delaunay tetrahedralization to put the VDF data on a uniform, linear velocity grid. To avoid colinear data point errors, we introduce a small, random jitter to the velocity data prior to the regridding[38]. The process for finding $\mathbf{GF}_{cor}$ for each VDF explained above uses one set of jitter values for each VDF (i.e., each iteration to reduce ζ uses the same jitter). We go through to calculate the velocity moments after applying the converged $\mathbf{GF}_{cor}$ for each VDF, a new jitter is calculated because the routine uses a random number generator. Given the small magnitude of the jitter values (i.e., $>10^{8}$ orders of magnitude smaller than any velocity), we initially assumed that the difference in the jitter values between the first and second step in our process would not affect $n_{e,int}$. However, we discovered that this was not so for ∼5500 VDFs in the final dataset (e.g., VDFs with $\zeta > 6.5\%$).

The source of the deviation is a a combination of uncertainties. We recall that the location of a velocity point relative to the speed equivalent of ϕ_{sc} matters greatly in the accuracy of the subsequent velocity moments, as shown by L. B. Wilson III et al. (2022). However, unlike in the example calculations done by L. B. Wilson III et al. (2022),

[34] Note that almost all of these specific choices in the methodology came about empirically from trial-and-error on 1000s of VDFs.

[35] Note that a lack of $n_{e,WAVES}$ or phi_{sc} would result in null $\mathbf{GF}_{cor}$ values as well.

[36] That is, the calculation of $\mathbf{GF}_{cor}$ is easily parallelized but would become a serial process if we computed the velocity moments directly after finding $\mathbf{GF}_{cor}$. Initial benchmark testing showed the two-step process to be much faster.

[37] There was no fitting or manual intervention here. Rather, the process required the user to input time ranges and run commands to initiate the software to either calibrate or calculate velocity moments. Then the results were examined superficially for glaring errors prior to the generation of temporary save files. After all VDFs were calibrated and moments calculated, a combined file was generated

[38] The magnitude of these jitters are at the floating point accuracy level or $\sim 10^{-6}$ km/s. They are determined using a random number generator with a random seed (i.e., the jitter values change for each VDF and between the first and second step in our two-step methodology).

we do not know the exact value of ϕ_{sc}. We also must contend with signal-to-noise ratio limitations in real data. The combination of these two effects likely resulted in final velocity moments satisfying $\zeta > 6.5\%$.

Of the 3,947,607 finite velocity moments in the dataset (see Section 2), we found that 750,650(18.79%) satisfied $\zeta \leq 1\%$ and 3,914,646(97.98%) satisfied $\zeta \leq 10\%$.

C. CONTRAST WITH OTHER ELECTRON DATASETS

In this appendix, we explain how the methodology for generating the data presented herein is different from other recent electron velocity moment datasets. Three of the four most recent electron velocity moment datasets are outlined in L. B. Wilson III et al. (2018) and L. B. Wilson III et al. (2023c) (called Set I[39]), C. S. Salem et al. (2023) (called Set II[40]), and S. D. Bale et al. (2013) (called Set IV[41]). The fourth examines electron velocity moments for a 50 day period in 1995, described in A. V. Eyelade et al. (2025) (called Set III[42]). Sets I and II use the *Wind*/3DP instrument while Set III relies on the SWE/VEIS instrument (K. W. Ogilvie et al. 1995). However, there are several important differences which we discuss below.

All of the data in Set I was taken prior to January 1, 2005. All of the data in Set II was taken prior to January 1, 1999. All of the data in Set III was taken in mid-1995. All of the data in Set IV was taken prior to 2003. This is important because for most of the VDFs in these datasets, $E_{min} > \phi_{sc}$. The reason being that *Wind* was passing through the terrestrial magnetosphere consistently, where $T_{e,j}$ is typically much larger than in the near-Earth solar wind. Thus, the 3DP instrument team set E_{min} to values ranging from 5.2 eV to 13.6 eV. The 3DP team reduced E_{min} to the 5.2 eV value after ∼February 1999 (i.e., after all of Set I). The E_{min} for SWE-VEIS for Set III was 13.9 eV, but that study ignored the first two energy bins. Therefore, a different method was devised to provide calibrated velocity moments that used ϕ_{sc} as a free parameter but did not directly calculate $\mathbf{GF}_{cor}$ (e.g., see C. S. Salem et al. 2001, 2023, for details). That is, they iteratively adjusted ϕ_{sc} until ζ was below some threshold and did not alter $\mathbf{GF}_{def}$. We cannot directly reproduce datasets I, II, or IV as they rely upon completely different algorithms and assumptions. Thus, we cannot directly compare the data from those intervals to that data generated for this two-part study. We can, and do, indirectly compare the results in a statistical manner in Paper II.

A second important distinction is that Set I and II both incorporated the EESA High detector (part of 3DP) to help constrain and improve the third velocity moment (i.e., heat flux). Both Set I and II derive the velocity moments from fits, which required a slightly larger energy range to constrain the heat flux-carrying electron population. Our estimates for ϕ_{sc} are much better constrained because $E_{min} < \phi_{sc}$, which allowed us to estimate $\mathbf{GF}_{cor}$. Thus, we did not need to incorporate EESA High data to calculate the electron heat flux tensor.

The third important distinction is that Sets I–IV all start from nonlinear least-squares fits of the electron VDF, and those fits are integrated[43] to determine total electron moments. Sets I, II, and IV fit to 1D cuts of the electron VDF, starting with the cut perpendicular to $\mathbf{B}_o$. The results from this fit are used to constrain the parallel cut fit and the combination of these results are compiled to construct a total fit for the entire VDF. It is worth noting that both the bi-Maxwellian and bi-kappa model functions used in the fitting process are not separable functions. Thus, the creators of Sets I, II, and IV imposed strict constraints on some fit parameters (e.g., $n_{e,int} = n_{e,WAVES}$). They fit to 1D cuts of the VDF because the algorithm is more numerically stable as there are fewer free parameters and fewer data points.

Set III fits to the 1D reduced VDFs rather than 1D cuts of the VDFs like in Sets I and II. Set III also imposes a zero net current constraint in the fitting process, which was not used for the velocity moments in this study.

In contrast, the velocity moments calculated herein are determined by performing a proper numerical integration scheme (i.e., three-dimensional Simpson's 1/3 Rule) on the calibrated 3D VDFs in units of phase space density. We do this in several steps. First we convert from raw counts to phase space density, as detailed in Appendix B. We then adjust the energies by ϕ_{sc}. The energy adjustment is done after unit conversion because phase space density is a Lorentz invariant (e.g., N. G. Van Kampen 1969). Then we integrate $f(\mathbf{v})$ in the standard velocity moment approach but we use a three-dimensional Simpson's 1/3 Rule for the numerical integration. The choice of method is actually very important. For instance, the Trapezoid Rule approach yields significantly less accurate moment results (e.g., L. B. Wilson III et al. 2022). The software is publicly available and open source (L. B. Wilson III 2021).

[39] There were ∼820,000 velocity moments between January 1, 1995 and December 31, 2004.

[40] There were ∼280,000 velocity moments between January 1, 1995 and December 31, 1998.

[41] There were ∼155,182 velocity moments in two, two-year intervals: 1995–1997 and 2001–2002.

[42] There were ∼65,850 SWE/VEIS velocity moments between May 15, 1995 and July 3, 1995.

[43] Note they also use a different numerical integration scheme than the Simpson's 1/3 Rule approach used herein. None of the 3DP velocity moments from the data herein depended upon any type of fitting function or process.

Despite the different algorithms, time ranges, and limitations in each approach, we do find consistency with the previous electron moment results (e.g., see S. D. Bale et al. 2013; C. S. Salem et al. 2023; L. B. Wilson III et al. 2018, 2023c). For instance, Paper II illustrates a remarkable agreement with C. S. Salem et al. (2023) despite the many differences in the method for calculating the velocity moments.

D. PUBLIC DATASET

In this appendix, we provide details about the public dataset that will result from this two-part study.

The calibrated electron velocity moments discussed herein will be archived[44] with NASA's Space Physics Data Facility (SPDF)[45] as common data format (CDF) binary files. The data are at the midpoint times of the 3DP VDFs, as is presented in this paper. That is, there will be a total of 3,996,051 unique timestamps in the public dataset, of which 3,947,607 have finite velocity moment solutions.

Below we list the CDF variable names and their definitions. The variables included in each CDF file will include (no particular order):

non-moment parameters

- 'EPOCH' : [N]-element (numeric) array of scalar Epoch (CDF TT2000 format) times
- 'QFLAG' : [N]-element (numeric) array of scalar quality flags defining the reliability of the data (see definitions below)
- 'B3_GSE' : [N,3]-element (numeric) array of 3-vector magnetic field data ($\mathbf{B}_o$ [nT]) in the GSE coordinate basis
- 'PHI_SC' : [N]-element (numeric) array of scalar floating electric potentials (ϕ_{sc} [eV])
- 'GF_COR' : [N,8]-element (numeric) array of anode-specific corrections for the 3DP detector ($\mathbf{GF}_{cor}$ [N/A])
- 'NE_WAV' : [N]-element (numeric) array of total electron number densities derived from the WAVES upper hybrid line ($n_{e,WAVES}$ [cm^{-3}])

velocity moments of $f(\mathbf{v})$

- 'NE_3DP' : [N]-element (numeric) array of scalar total electron number densities ($n_{e,int}$ [cm^{-3}]) from the zeroth velocity moment
- 'UE_3DP' : [N,3]-element (numeric) array of 3-vector electron bulk flow velocities ($\mathbf{V}_{oe}$ [km s^{-1}]) from the first velocity moment
- 'PS_3DP' : [N]-element (numeric) array of scalar total electron thermal pressure (P_{Te} [eV cm^{-3}]) from the second velocity moment
- 'AE_3DP' : [N]-element (numeric) array of scalar electron temperature anisotropy (A_e [N/A]) from the second velocity moment
- 'TE_3DP' : [N,3]-element (numeric) array of total electron temperature components ($T_{e,j}$ [eV]) from the second velocity moment in the FAC coordinate basis (parallel, perpendicular, total)
- 'QE_3DP' : [N,3]-element (numeric) array of electron heat flux ($\mathbf{q}_e$ [μW m^{-2}]) from the third velocity moment in the FAC coordinate basis (perpendicular 1, perpendicular2, parallel)
- 'QN_3DP' : [N,3]-element (numeric) array of normalized electron heat flux ($\mathbf{q}_e/q_{eo}$ [N/A]) from the third velocity moment in the FAC coordinate basis (perpendicular 1, perpendicular2, parallel)

lower bound values from velocity moments of $f(\mathbf{v}) - \delta f(\mathbf{v})$

- 'DNE3DL' : [N]-element (numeric) array of scalar total electron number densities ($n_{e,int}$ [cm^{-3}]) from the zeroth velocity moment
- 'DUE3DL' : [N,3]-element (numeric) array of 3-vector electron bulk flow velocities ($\mathbf{V}_{oe}$ [km s^{-1}]) from the first velocity moment
- 'DPS3DL' : [N]-element (numeric) array of scalar total electron thermal pressure (P_{Te} [eV cm^{-3}]) from the second velocity moment
- 'DAE3DL' : [N]-element (numeric) array of scalar electron temperature anisotropy (A_e [N/A]) from the second velocity moment
- 'DTE3DL' : [N,3]-element (numeric) array of total electron temperature components ($T_{e,j}$ [eV]) from the second velocity moment in the FAC coordinate basis (parallel, perpendicular, total)

[44] The data will be released when the papers are accepted.

[45] https://spdf.gsfc.nasa.gov

- 'DQE3DL' : [N,3]-element (numeric) array of electron heat flux ($\mathbf{q}_{e}$ [μW m^{-2}]) from the third velocity moment in the FAC coordinate basis (perpendicular 1, perpendicular2, parallel)
- 'DQN3DL' : [N,3]-element (numeric) array of normalized electron heat flux ($\mathbf{q}_{e}/q_{eo}$ [N/A]) from the third velocity moment in the FAC coordinate basis (perpendicular 1, perpendicular2, parallel)

upper bound values from velocity moments of $f\left(\mathbf{v}\right) + \delta f\left(\mathbf{v}\right)$

- 'DNE3DU' : [N]-element (numeric) array of scalar total electron number densities ($n_{e,int}$ [cm^{-3}]) from the zeroth velocity moment
- 'DUE3DU' : [N,3]-element (numeric) array of 3-vector electron bulk flow velocities ($\mathbf{V}_{oe}$ [km s^{-1}]) from the first velocity moment
- 'DPS3DU' : [N]-element (numeric) array of scalar total electron thermal pressure (P_{Te} [eV cm^{-3}]) from the second velocity moment
- 'DAE3DU' : [N]-element (numeric) array of scalar electron temperature anisotropy (A_{e} [N/A]) from the second velocity moment
- 'DTE3DU' : [N,3]-element (numeric) array of total electron temperature components ($T_{e,j}$ [eV]) from the second velocity moment in the FAC coordinate basis (parallel, perpendicular, total)
- 'DQE3DU' : [N,3]-element (numeric) array of electron heat flux ($\mathbf{q}_{e}$ [μW m^{-2}]) from the third velocity moment in the FAC coordinate basis (perpendicular 1, perpendicular2, parallel)
- 'DQN3DU' : [N,3]-element (numeric) array of normalized electron heat flux ($\mathbf{q}_{e}/q_{eo}$ [N/A]) from the third velocity moment in the FAC coordinate basis (perpendicular 1, perpendicular2, parallel)

The quality flag values, 'QFLAG', are determined by the parameter ζ (see Appendix A) and a few other physical constraints. We define the value of 1 to be the best and 8 to be the worst. The definitions are as follows:

$\mathcal{B} \equiv (V_{oe,x} \geq -50\ km/s) \vee (|q_{e,j}|/q_{eo} \geq 1) \vee (T_{e,j} \leq 1\ eV)$
$\mathcal{G} \equiv (V_{oe,x} < -50\ km/s) \wedge (|q_{e,j}|/q_{eo} < 1) \wedge (T_{e,j} > 1\ eV)$
$8 \equiv (\zeta > 20\%) \vee \mathcal{B}$
$7 \equiv (10\% < \zeta \leq 20\%) \wedge \mathcal{G}$
$6 \equiv (8\% < \zeta \leq 10\%) \wedge \mathcal{G}$
$5 \equiv (6\% < \zeta \leq 8\%) \wedge \mathcal{G}$
$4 \equiv (5\% < \zeta \leq 6\%) \wedge \mathcal{G}$
$3 \equiv (3\% < \zeta \leq 5\%) \wedge \mathcal{G}$
$2 \equiv (1\% < \zeta \leq 3\%) \wedge \mathcal{G}$
$1 \equiv (0\% < \zeta \leq 1\%) \wedge \mathcal{G}$

The number of values for each quality flag and the respective percentages are shown below:

8 : 1,021 (0.03%)
7 : 1,975 (0.05%)
6 : 2,513 (0.06%)
5 : 13,134 (0.33%)
4 : 84,118 (2.11%)
3 : 1,543,973 (38.64%)
2 : 1,485,396 (37.18%)
1 : 742,221 (18.58%)

Thus, 96.94% of the data have quality flags less than eight.

REFERENCES

Bale, S. D., Pulupa, M., Salem, C., Chen, C. H. K., & Quataert, E. 2013, Astrophys. J. Lett., 769, L22, doi: 10.1088/2041-8205/769/2/L22

Besse, A. L., & Rubin, A. G. 1980, J. Geophys. Res., 85, 2324, doi: 10.1029/JA085iA05p02324

Boehm, M. H., Carlson, C. W., McFadden, J. P., et al. 1994, J. Geophys. Res., 99, 21361, doi: 10.1029/94JA01766

Bonnell, J. W., Mozer, F. S., Delory, G. T., et al. 2008, Space Sci. Rev., 141, 303, doi: 10.1007/s11214-008-9469-2

Bordoni, F. 1971, Nucl. Inst. & Meth., 97, 405, doi: 10.1016/0029-554X(71)90300-4

Bougeret, J.-L., Kaiser, M. L., Kellogg, P. J., et al. 1995, Space Sci. Rev., 71, 231, doi: 10.1007/BF00751331

Brehm, B., Grosser, J., Ruscheinski, T., & Zimmer, M. 1995, Meas. Sci. Technol., 6, 953, doi: 10.1088/0957-0233/6/7/015

Cara, A., Lavraud, B., Fedorov, A., et al. 2017, J. Geophys. Res., 122, 1439, doi: 10.1002/2016JA023269

Carlson, C. W., Curtis, D. W., Paschmann, G., & Michael, W. 1982, Adv. Space Res., 2, 67, doi: 10.1016/0273-1177(82)90151-X

Carlson, C. W., & McFadden, J. P. 1998, in Geophys. Monogr. Ser., Vol. 102, Measurement Techniques in Space Plasmas: Particles, ed. R. F. Pfaff, J. E. Borovsky, & D. T. Young (Washington, D.C.: AGU), 125–140, doi: 10.1029/GM102p0125

Collinson, G. A., & Kataria, D. O. 2010, Meas. Sci. Technol., 21, 105903, doi: 10.1088/0957-0233/21/10/105903

De Keyser, J., Lavraud, B., Přech, L., et al. 2018, Ann. Geophys., 36, 1285, doi: 10.5194/angeo-36-1285-2018

De Marco, R., Marcucci, M. F., Bruno, R., et al. 2016, J. Instrum., 11, C08010, doi: 10.1088/1748-0221/11/08/C08010

Diaz-Aguado, M. F., Bonnell, J. W., Bale, S. D., Wang, J., & Gruntman, M. 2021, J. Geophys. Res., 126, e2020JA028688, doi: 10.1029/2020JA02868810.1002/essoar.10504358.1

Eyelade, A. V., Zenteno-Quinteros, B., Moya, P. S., et al. 2025, Astron. & Astrophys., 702, A198, doi: 10.1051/0004-6361/202555368

Fränz, M., & Harper, D. 2002, Planet. Space Sci., 50, 217

Garrett, H. B. 1981, Rev. Geophys. Space Phys., 19, 577

Gary, S. P., Skoug, R. M., & Daughton, W. 1999, Phys. Plasmas, 6, 2607, doi: 10.1063/1.873532

Geach, J., Schwartz, S. J., Génot, V., et al. 2005, Ann. Geophys., 23, 931, doi: 10.5194/angeo-23-931-2005

Génot, V., & Schwartz, S. 2004, Ann. Geophys., 22, 2073, doi: 10.5194/angeo-22-2073-2004

Gershman, D. J., Dorelli, J. C., F.-Viñas, A., & Pollock, C. J. 2015, J. Geophys. Res., 120, 6633, doi: 10.1002/2014JA020775

Gershman, D. J., Gliese, U., Dorelli, J. C., et al. 2016, J. Geophys. Res., 121, 10005, doi: 10.1002/2016JA022563

Gershman, D. J., Avanov, L. A., Boardsen, S. A., et al. 2017, J. Geophys. Res., 122, 11548, doi: 10.1002/2017JA024518

Gershman, D. J., Dorelli, J. C., Avanov, L. A., et al. 2019, J. Geophys. Res., 124, 10,345, doi: 10.1029/2019JA026980

Goruganthu, R. R., & Wilson, W. G. 1984, Rev. Sci. Inst., 55, 2030, doi: 10.1063/1.1137709

Grard, R., Knott, K., & Pedersen, A. 1983, Space Sci. Rev., 34, 289, doi: 10.1007/BF00175284

Grard, R. J. L. 1973, J. Geophys. Res., 78, 2885, doi: 10.1029/JA078i016p02885

Kasper, J. C., Lazarus, A. J., Steinberg, J. T., Ogilvie, K. W., & Szabo, A. 2006, J. Geophys. Res., 111, 3105, doi: 10.1029/2005JA011442

Lai, S. T., Martinez-Sanchez, M., Cahoy, K., et al. 2017, IEEE Trans. Plasma Sci., 45, 2875, doi: 10.1109/TPS.2017.2751002

Lavraud, B., & Larson, D. E. 2016, J. Geophys. Res., 121, 8462, doi: 10.1002/2016JA022591

Lepping, R. P., Acũna, M. H., Burlaga, L. F., et al. 1995, Space Sci. Rev., 71, 207, doi: 10.1007/BF00751330

Lin, R. P., Anderson, K. A., Ashford, S., et al. 1995, Space Sci. Rev., 71, 125, doi: 10.1007/BF00751328

Mackenzie, J. D. 1977,, 1.0 Materials Department, University of California, Los Angeles. https://apps.dtic.mil/sti/citations/ADA055251

Martinović, M. M., Klein, K. G., Gramze, S. R., et al. 2020, J. Geophys. Res., 125, e28113, doi: 10.1029/2020JA028113

McFadden, J. P., Carlson, C. W., Larson, D., et al. 2008a, Space Sci. Rev., 141, 477, doi: 10.1007/s11214-008-9433-1

McFadden, J. P., Carlson, C. W., Larson, D., et al. 2008b, Space Sci. Rev., 141, 277, doi: 10.1007/s11214-008-9440-2

Meyer-Vernet, N., & Perche, C. 1989, J. Geophys. Res., 94, 2405, doi: 10.1029/JA094iA03p02405

Ogilvie, K. W., Chornay, D. J., Fritzenreiter, R. J., et al. 1995, Space Sci. Rev., 71, 55, doi: 10.1007/BF00751326

Pedersen, A. 1995, Ann. Geophys., 13, 118, doi: 10.1007/s00585-995-0118-8

Pulupa, M. P., Bale, S. D., Salem, C., & Horaites, K. 2014, J. Geophys. Res., 119, 647, doi: 10.1002/2013JA019359

Salem, C. S., Bosqued, J.-M., Larson, D. E., et al. 2001, J. Geophys. Res., 106, 21701, doi: 10.1029/2001JA900031

Salem, C. S., Hubert, D., Lacombe, C., et al. 2003, Astrophys. J., 585, 1147, doi: 10.1086/346185

Salem, C. S., Pulupa, M. P., Bale, S. D., & Verscharen, D. 2023, Astron. & Astrophys., 675, A162, doi: 10.1051/0004-6361/202141816

Sandel, B. R., Broadfoot, A. L., & Shemansky, D. E. 1977, Appl. Optics, 16, 1435, doi: 10.1364/AO.16.001435

Schwartz, S. J., Goodrich, K. A., Wilson III, L. B., et al. 2022, J. Geophys. Res., 127, e2022JA030637, doi: 10.1029/2022JA030637

Scime, E. E., Phillips, J. L., & Bame, S. J. 1994, J. Geophys. Res., 99, 14769, doi: 10.1029/94JA00489

Scudder, J. D., Cao, X., & Mozer, F. S. 2000, J. Geophys. Res., 105, 21281, doi: 10.1029/1999JA900423

Song, P., Zhang, X. X., & Paschmann, G. 1997, Planet. Space Sci., 45, 255, doi: 10.1016/S0032-0633(96)00087-6

Van Kampen, N. G. 1969, Physica, 43, 244, doi: 10.1016/0031-8914(69)90005-6

Whipple, E. C. 1981, Rep. Progr. Phys., 44, 1197, doi: 10.1088/0034-4885/44/11/002

Wilson, R. J. 2015, Earth Space Sci., 2, 201, doi: 10.1002/2014EA000090

Wilson III, L. B. 2021,, 1.0.2 Zenodo, doi: 10.5281/zenodo.6141586

Wilson III, L. B., Bale, S. D., Stevens, M. L., et al. 2026, Astrophys. J.

Wilson III, L. B., Cattell, C., Kellogg, P. J., et al. 2007, Phys. Rev. Lett., 99, 041101, doi: 10.1103/PhysRevLett.99.041101

Wilson III, L. B., Goodrich, K. A., Turner, D. L., et al. 2022, Front. Astron. Space Sci., 9, 1063841, doi: 10.3389/fspas.2022.1063841

Wilson III, L. B., Salem, C. S., & Bonnell, J. W. 2023a, Astrophys. J. Suppl., 269, 10, doi: 10.3847/1538-4365/ad0633

Wilson III, L. B., Salem, C. S., & Bonnell, J. W. 2023b,, 1.0 Zenodo, doi: 10.5281/zenodo.8364797

Wilson III, L. B., Stevens, M. L., Kasper, J. C., et al. 2018, Astrophys. J. Suppl., 236, 41, doi: 10.3847/1538-4365/aab71c

Wilson III, L. B., Chen, L.-J., Wang, S., et al. 2019a, Astrophys. J. Suppl., 245, doi: 10.3847/1538-4365/ab5445

Wilson III, L. B., Chen, L.-J., Wang, S., et al. 2019b, Astrophys. J. Suppl., 243, doi: 10.3847/1538-4365/ab22bd

Wilson III, L. B., Brosius, A. L., Gopalswamy, N., et al. 2021, Rev. Geophys., 59, e2020RG000714, doi: 10.1029/2020RG000714

Wilson III, L. B., Stevens, M. L., Kasper, J. C., et al. 2023c, Astrophys. J. Suppl., 269, 12, doi: 10.3847/1538-4365/ad07de

Wiza, J. L. 1979, Nucl. Instr. Meth., 162, 587, doi: 10.1016/0029-554X(79)90734-1

Zheng, X., Martinović, M. M., Klein, K. G., et al. 2026, J. Geophys. Res., 131, e2025JA034176, doi: 10.1029/2025JA034176